

Nanoscale

Accepted Manuscript



This is an *Accepted Manuscript*, which has been through the Royal Society of Chemistry peer review process and has been accepted for publication.

Accepted Manuscripts are published online shortly after acceptance, before technical editing, formatting and proof reading. Using this free service, authors can make their results available to the community, in citable form, before we publish the edited article. We will replace this *Accepted Manuscript* with the edited and formatted *Advance Article* as soon as it is available.

You can find more information about *Accepted Manuscripts* in the [Information for Authors](#).

Please note that technical editing may introduce minor changes to the text and/or graphics, which may alter content. The journal's standard [Terms & Conditions](#) and the [Ethical guidelines](#) still apply. In no event shall the Royal Society of Chemistry be held responsible for any errors or omissions in this *Accepted Manuscript* or any consequences arising from the use of any information it contains.

ARTICLE

Single Nanowire Manipulation within Dielectrophoretic Force Fields in the Sub-Crossover Frequency Regime

Cite this: DOI: 10.1039/x0xx00000x

N. K. R. Palapati,^a E. Pomerantseva^b and A. Subramanian^{a,*}Received 00th January 2012,
Accepted 00th January 2012

DOI: 10.1039/x0xx00000x

www.rsc.org/

This paper presents the quantitative relationship between the control parameters of a dielectrophoretic (DEP) force field and the resulting electrokinetic region of influence experienced by individual nanowires (NWs) in colloidal suspensions. Our results show that DEP operation at sub-crossover frequencies, which are defined as frequencies slightly below the transition from positive-to-negative DEP, offers a suitable but previously unexplored performance regime for single NW manipulation and assembly. The low-magnitude DEP forces at these frequencies, which are estimated to be 8 orders of magnitude smaller as compared to near-DC frequencies, provide an efficient avenue to controllably extend electrokinetic influence on suspension volumes that present isolated NWs. These results are demonstrated using α -phase manganese dioxide NWs as a model one-dimensional construct. Based on experimentally extracted values for the NW intrinsic conductivity and dielectric permittivity, we employ computational models to explain each of the performance regimes observed in this nanoassembly system. In addition, we use a new approach to estimate the concentration of a NW suspension from experimentally observed data for deposition yields.

Introduction

Since the advent of carbon nanotubes in the 1990s, an increasing number of new material systems have been synthesized in one-dimensional (1-D) form factors such as nanowires (NWs) and nanotubes (NTs). Most nanomaterial synthesis techniques typically result in an end-product that contains the NWs / NTs either as macroscopic agglomerates in powder form, or as dense, aligned forests on substrates. Isolation and manipulation of individual 1-D elements from their respective agglomerated precursors, and their integration into functional nanostructures is essential for two reasons: (1) to understand the unique structure-property-performance relationships that emerge in these nanoscopic objects,¹ and (2) to realize functional devices for application areas such as sensing, nanoelectromechanical systems, energy storage, fuel cells and nanoelectronics.²⁻⁵

One technique for the integration of 1-D elements into nanostructures and nanodevices is their assembly by dielectrophoresis (DEP)⁴⁻¹⁹ on substrates such as silicon. DEP relies on the forces exerted by spatially non-uniform electric fields on polarizable objects to manipulate NWs / NTs, which are suspended either in solvents or in a surfactant stabilized aqueous medium. If the nano-objects are more polarizable than the suspension medium, then the induced dipole along their long axis will experience a DEP force that pushes it towards the electric field maxima. This represents the positive DEP regime

and occurs at frequencies below a characteristic threshold called the crossover frequency. At frequencies above this crossover threshold, the nano-object becomes less polarizable as compared to the medium and is manipulated towards the electric field minima. The electric field is typically generated by a potential applied between nano- or microfabricated electrode pairs on silicon chips, onto which the nano-objects are eventually assembled by operating in the positive DEP regime. This approach has been employed to assemble 1-D nano-objects based on diverse material systems. This is because DEP forces are exerted on any object as long as it has a sufficiently higher polarizability with respect to the suspension medium at the excitation frequency. Past reports, which have included contributions from the authors of this article, have demonstrated DEP assembly of material systems such as carbon nanotubes,⁵⁻⁹ silicon nanowires,¹¹⁻¹³ rhodium nanowires,¹³ manganese dioxide nanowires,⁴ gold nanowires,¹⁶ and lithium iron phosphate nanowires,¹⁷ among others.

A key consideration with the DEP integration of nanomaterials is the ability to localize single NWs or NTs from their colloidal suspension and yield their deposition on to the assembly electrodes. While most earlier reports demonstrated assembly of multiple or bundles of nanowires at the deposition locations,²⁰⁻²² there have since been many reports on successful demonstration of single particle DEP assembly, though with varying yields.⁴⁻¹⁹ Some of these single particle assembly methods, particularly ones with higher deposition yields, have

employed additional steps / processes beyond DEP manipulation.^{11,13,14,23} For instance, ref. [13] has employed pre-defined target deposition sites for DEP through lithographic patterning of photoresist wells, followed by a post-assembly resist lift-off process to selectively remove NWs, which were assembled at unwanted locations.

These efforts towards DEP integration of single NWs will benefit from quantitative strategies for precise control of the electrokinetic region of influence (ROI, or the extent of space from which the NWs can be successfully assembled / captured) through the use of deposition parameters such as assembly voltage, frequency and time. However, there has been no quantitative study so far to understand this relationship between the deposition parameters and the resultant ROI. This paper addresses this knowledge gap, and paves the way for predictive manipulation of single nanowire constructs in order to successfully trap them at target locations. More importantly, we show for the first time that operation within a low assembly force-field regime, which is characteristic of sub-crossover frequencies (near the transition from positive-to-negative DEP), provides better avenues for controllable modulation of the electrokinetic ROI as compared to near-DC frequencies. Furthermore, we present the quantitative impact of assembly bias and time on the ROI at these sub-crossover frequencies. Using experimentally extracted values for the NW conductivity and permittivity, we employ computational models to both, explain and gain further insights into these experimentally observed results. This includes a new approach for determining the NW concentration in its suspension.

Experimental

Hydrothermally grown α -MnO₂ NWs²⁴ were used as a model

one-dimensional system in these nanoassembly experiments. This material system was chosen as a part of our efforts to understand the ionic intercalation mechanisms within their crystalline tunnels for lithium-ion battery applications. A colloidal suspension is created by sonicating a sub-milligram scale quantity of the NWs in 20ml of ethanol for a period of ~10 minutes. The on-chip DEP platform is schematically shown in Fig. 1.⁴ A silicon chip with a 200nm thick film of silicon nitride serves as the starting substrate. We define arrays of gold nanoelectrode pairs using electron beam lithography followed by metal deposition and resist lift-off. The electrodes are made of gold with a chromium adhesion layer. The electrodes on one side of the array are all wired to a common contact pad, and the DEP bias is applied to this pad (Fig. 1(a-b)). The opposing electrodes on the right are all traced to their own individual pads. During DEP, these electrodes are held at a floating potential, while the AC ground is connected to the backside silicon substrate.^{4,6,21} The left electrode, right electrode and the backside gate electrode are called as biasing (B), floating (F) and gate (G) electrodes, respectively.

In order to perform DEP, we apply an AC bias (V_{AC}) between electrodes B and G, while placing a droplet of the NW suspension in ethanol on the surface of the chip (Fig. 1(a)). The AC bias creates an electric field, which is non-uniform in space, in the region surrounding the electrodes. If the NWs are more polarizable with respect to the ethanol medium, then the induced dipole along their long axis will line up along field lines (electro-orientation) and experience a DEP force that pushes it towards the electric field maxima located on the chip surface. This represents the positive DEP regime and occurs at frequencies below the crossover frequency (f_{CO}) for the NW material / suspension. At frequencies above f_{CO} , the NW becomes less polarizable as compared to the medium and is

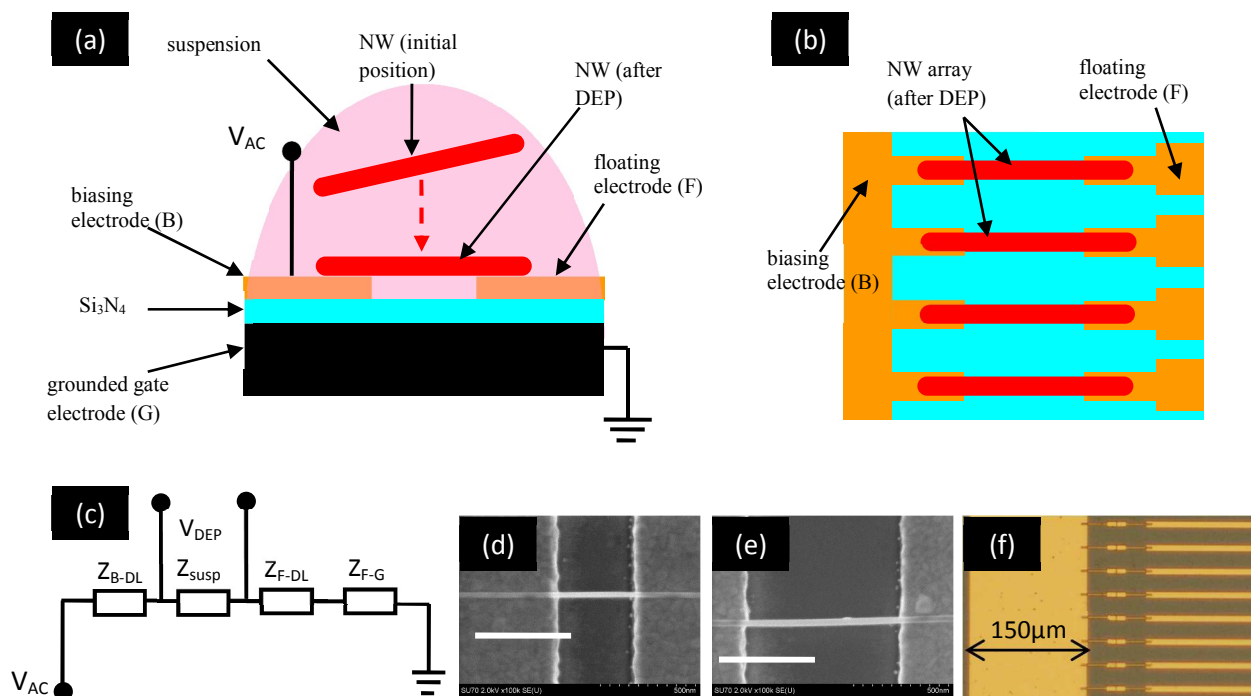


Figure 1. (a-b) Cross-sectional and top-view schematics of the on-chip electrokinetic nanomanipulation platform. (c) Equivalent electrical circuit showing the effective DEP bias (V_{DEP}), which is the voltage that appears across the suspension. (d-e) SEM images of the single α -MnO₂ NWs assembled across electrode pairs with gaps of 400nm and 800nm, respectively. Scale bars indicate 500nm. (f) An optical microscopy image of the electrode array design. In this image, the design width of the common bond pad for the left electrodes in the array measures 150 μ m.



Figure 2. (a) SEM image of an assembled nanowire with arrows pointing to top-side EBID Pt contacts. (b) AFM image of a representative NW. (c) I-V plots from 2 nanowire samples. These are used to extract the contact resistance and NW conductivity to be 182.2 S/m and 145.7k Ω , respectively.

manipulated towards the electric field minima. After the pre-determined assembly time, we turn off the assembly bias and dry the chip with a N₂ gun, after rinsing it in ethanol. After the assembly process, the NWs remain anchored in place due to the van der Waals interactions with the electrode surface. In our discussions on these experiments, we define two types of electrokinetic ROI for any given DEP condition: (1) an axial ROI, which represents the farthest distance along a given axis from which a NW will be manipulated to the electrode surface, and (2) a volumetric ROI, which represents the largest hemispherical volume (centered about the electrodes) within which a NW will be manipulated to the electrode surface for the given deposition conditions.

The equivalent circuit for the DEP system consists of three impedance components in series (Fig. 1(c)): the capacitive coupling between G and F (Z_{F-G}), the impedance offered by the suspension between B and F (Z_{susp}), and the grouped electrical double layer capacitance (from Z_{B-DL} and Z_{F-DL} contributions at electrodes B and F, respectively).⁶ The effective assembly bias experienced by the NWs, V_{DEP} , depends on the relative magnitudes of these impedance components (Fig. 1(c)). In our experiments, we employ chip designs with an array of 100 electrode pairs. We define the yield for a certain type of deposition condition (such as single or multiple NWs) as the percentage of these 100 locations, which exhibited that condition after assembly.

The polarizability of the NWs in the ethanol suspension is determined by the following components: the real permittivity (ϵ_{NW}) and conductivity (σ_{NW}) of the NWs, and the real permittivity (ϵ_{m}) and conductivity (σ_{m}) for the suspending medium, i.e., ethanol. While the values of these parameters for ethanol are known from literature,²⁵ we have used an experimental approach to extract these values for the α -MnO₂ NWs. Two DEP-assembled NW samples, with different suspended lengths between the assembly electrodes, were clamped at their distal ends on the top-side using electron beam induced deposition (EBID) of platinum (Pt) contacts (Fig. 2(a)). This top-side contact is established to reduce the contact resistance at the NW-gold interface. The two terminal resistances of these devices are obtained from their current-voltage (I-V) measurements, which were performed with a Keithley 2636B source-meter. This two terminal resistance (R_{2T}) is given as:⁸

$$R_{2T} = 2R_c + \frac{l}{\sigma_{\text{NW}}A} \quad (1)$$

where R_c , l and A represent the NW-metal contact resistance, NW length and NW cross-sectional area, respectively. By performing the measurements on two separate NW samples with different NW diameters and lengths, we extract the two unknowns in the above equation, i.e., R_c and σ_{NW} . Furthermore, the crossover frequency depends on the conductivity and dielectric permittivity of the NW sample. From experimental measurements of f_{CO} and from the computed value of σ_{NW} , we then extract the value of ϵ_{NW} (as discussed later).

Results and Discussion

Representative SEM images of single α -MnO₂ NWs assembled across electrodes is shown in Fig. 1(d-e), while the electrode array design is shown in panel 'f' of this image. Fig. 2(a-b) show SEM and AFM images of NW samples after the post-assembly, Pt EBID deposition step. I-V measurements obtained from two NWs of different sizes are shown in Fig. 2(c). In this measurement, the first NW (with a lower two-terminal resistance) was 412nm long and had a diameter of 19nm, while the second NW sample was 759nm long and had a diameter of 16nm. By inserting this data in Eq. (1), we obtain the intrinsic conductivity and NW-metal contact resistance to be 182.2 S/m and 145.7k Ω , respectively. It is important to note that the top-side metallization results in a contact impedance, which is an order of magnitude smaller than the two-terminal resistance ($> 2 \text{ M}\Omega$) observed in our devices. Furthermore, the extracted value of the intrinsic NW conductivity is similar to the 101 S/m value, which was reported previously for 15% Ba-stabilized α -MnO₂ thin film samples.²⁶

At a given deposition condition, the time-averaged value of the dielectrophoretic force acting on a NW ($\langle F_{\text{DEP}} \rangle$) is given by^{7, 27, 28}

$$\langle F_{\text{DEP}} \rangle = \frac{3}{2} \pi r^2 l \epsilon_m \text{Re}\{K\} \nabla(\mathbf{E} \cdot \mathbf{E}^*) \quad (2)$$

where r , \mathbf{E} and \mathbf{E}^* represent the NW radius, the applied electric field, and the complex conjugate of the electric field, respectively. In the above model, the NW is approximated as a prolate ellipsoid with a length much greater than its diameter. In the above equation, the complex parameter K , or the Clausius-Mossotti factor, indicates the relative polarizability of the NW with respect to the medium and is defined as²⁹

$$K = \frac{\tilde{\epsilon}_{\text{NW}} - \tilde{\epsilon}_{\text{m}}}{\tilde{\epsilon}_{\text{m}}} \quad (3)$$

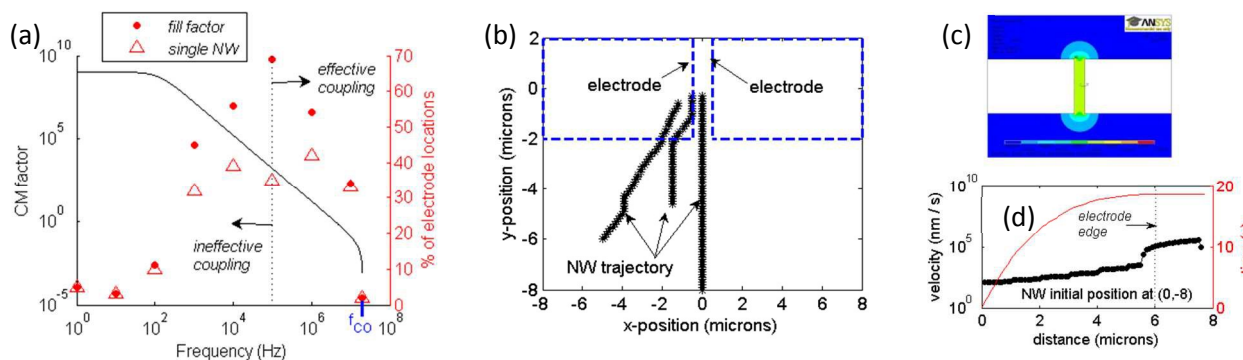


Figure 3. (a) Clausius-Mossotti factor and experimentally observed NW deposition metrics are plotted as a function of frequency. The crossover frequency is highlighted on the frequency axis in blue. (b) The trajectory assumed by NWs that start at three different initial positions. The model assumed DEP conditions of 800nm electrode gap, NW with 10nm diameter and $3\mu\text{m}$ length, V_{DEP} of $1V_{\text{p-p}}$ at 1MHz and 2 minute deposition time. (c) The electric field distribution, which is computed using an ANSYS finite-element model and is used as an input to the MATLAB model of panel 'b'. (d) NW velocity and time lapsed as a function of its position in the trajectory. This is shown for the NW of 'b' that starts at $(0, -8\mu\text{m})$.

where $\tilde{\epsilon}_{\text{NW}}$ and $\tilde{\epsilon}_m$ represent the complex permittivity of the NW and the ethanol medium, respectively. It is important to note that the complex permittivity, $\tilde{\epsilon}$, of an object is related to its real dielectric permittivity (ϵ), conductivity (σ) and the field frequency (ω) by the following relation:

$$\tilde{\epsilon} = \epsilon - i \frac{\sigma}{\omega} \quad (4)$$

At frequencies below f_{CO} , the real part of K is positive (in Eq. (2)) and results in positive DEP or manipulation of the NWs towards the electric field maxima (located on the electrode surface). Otherwise, negative DEP regime occurs and the NWs are pushed towards regions of electric field minima, resulting in no deposition on the electrodes. Assuming a constant magnitude for the electric field along the length of the NW dipole and a spatially invariant phase,^{6, 7, 30, 31} Eq. (2) can be written as

$$\langle \mathbf{F}_{\text{DEP}} \rangle = \frac{3}{2} \pi r^2 l \epsilon_m \text{Re}\{K\} \nabla |\mathbf{E}|^2 \quad (5)$$

The experimental results from this frequency-dependent DEP behavior of the $\alpha\text{-MnO}_2$ NWs in an ethanol medium is shown in Fig. 3(a). The experiments were carried out by varying the excitation frequency, while keeping the bias voltage and deposition time constant at $1V_{\text{p-p}}$ (peak-to-peak) and 2 minutes, respectively. In these plots, the term 'fill-factor' represents the percentage of electrode locations (within the 100 electrode array) that resulted in some form of NW deposition, which includes locations with single, multiple, overlapping and cantilevered NWs. Fill-factor provides insights into the number of electrode locations in the array that have one or more nanowires within the volumetric ROI of the electric field. On the other hand, the 'single NW' plot represents the percentage of electrode locations within the array that yielded exactly one NW bridging the electrode pairs. This represents the number of electrode locations in the array that have exactly one NW in their volumetric ROI of the electric field. From these results, we see that the DEP fill-factor is low at near-DC frequencies and it increases to a maximum at a 100KHz field. Beyond 100 KHz, the fill-factor monotonically decreases with frequency until 20MHz, when it drops to a value of 2%. Beyond 20MHz, we did not observe any NW deposition at all. Thus, f_{CO} for our system occurs at 20MHz. While σ_{NW} was previously determined from IV measurements to be 182.2S/m , the values of ϵ_m and σ_m are known to be $2.17 \times 10^{-10} \text{F/m}$ and $1.35 \times 10^{-7} \text{S/m}$, respectively.²⁵ By inserting these values for f_{CO} , ϵ_{NW} , ϵ_m and σ_m

in Eq. (3), we have employed a MATLAB code to solve for the dielectric permittivity of the NW and obtained this to be $2.07 \times 10^{-10} \text{F/m}$. This corresponds to a relative permittivity of 23.5 for $\alpha\text{-MnO}_2$ NWs and agrees with measurements previously reported for $\alpha\text{-MnO}_2$ nanorods (~ 26 , as estimated at 300K from a plot of permittivity vs. temperature).³²

Using these experimentally estimated values for ϵ_{NW} and σ_{NW} , we have plotted the clausius-Mossotti factor, K , as a function of AC frequency in Fig. 3(a). Since \mathbf{F}_{DEP} is proportional to K (Eq. (5)), the volumetric ROI and fill-factor are expected to scale as a function of K . We find that our experimental results are in agreement with the numerically computed profile for K at frequencies above 100KHz. On the other hand, we observe very little NW deposition at lower frequencies, even though the DEP force is estimated to be 8 to 10 orders of magnitude higher at these frequencies as compared to that at 20MHz. For example, the values of K are estimated to be 6.45×10^8 and 0.1218 at 100Hz and 10MHz, respectively (note the log scale of the left y-axis in Fig. 3(a)). This deviation in experimental results from the computational models at frequencies below 100KHz is explained by the ineffective coupling between V_{DEP} and V_{AC} (see Fig. 1(d) for voltage definitions). We attribute this behavior to the dominating influence of both, the insulation layer capacitance and the electrical double-layer capacitance at frequencies below a characteristic threshold, which is determined by the medium conductivity, permittivity and Debye length.³³ At frequencies below this threshold, the system has sufficient time to develop an electric double-layer at the electrode-suspension interfaces, resulting in $V_{\text{DEP}} \ll V_{\text{AC}}$. As a result, the DEP force is too small at the lower frequencies to achieve substantive deposition. On the other hand, the electrical double-layer capacitance vanishes at frequencies above this characteristic threshold, and there is efficient coupling between the floating electrodes and the grounded back gate, i.e., $V_{\text{DEP}} = V_{\text{AC}}$. While a direct quantification of the contributions from individual impedance components and the resulting threshold frequency has been obtained in the past from impedance spectroscopy techniques,⁶ our analysis has relied on the comparison between experimentally observed dependence of deposition results on the frequency and the computationally estimated profile for electrokinetic force scaling.

In order to gain further insights into the significance of the observed single NW and fill-factor yields, it is essential to

understand the NW response to the DEP force field in terms of its positional trajectory, velocity and response time. Based on hydrodynamic models developed by Hardings and Small,³⁴⁻³⁶ the average friction factor, f , experienced by the prolate ellipsoidal NWs is given as

$$f = \frac{3\pi\eta l}{\ln(l/r)} \quad (6)$$

where η represents the viscosity of ethanol. The velocity of the NW, v , in response to the excitation force at any location within the field is computed as

$$v = F_{DEP}/f \quad (7)$$

In the above equation, we have neglected the contribution from inertial effects of the NW. This is because, in our system, the characteristic time constant ($\tau = m/f$, where 'm' is the NW mass)⁶ for inertial effects is significantly smaller than the experimental NW capture time. For example, in the case of a representative NW with a 20nm diameter and 3 μ m length, τ is calculated as 0.8 nanoseconds (using a crystallographic mass density of 4.34 kg/m³ for α -MnO₂) and remains 11 to 12 orders of magnitude smaller than the experimental deposition time of 2 to 8 minutes.

We have employed 2-D finite-element models in ANSYS to compute the electric field distribution around the electrodes for a given potential across the electrodes (Fig. 3(c)). Based on Eqs. (2-7), we have created a MATLAB computational code to convert the electric field distribution into DEP force and NW velocity maps at each location within the workspace. This

model enables us to compute the trajectory assumed by a NW for a given initial position within the electrokinetic field (Fig. 3(b)). Furthermore, we calculate the NW velocity and the time taken by it to navigate along this trajectory. For example, Fig. 3(d) plots the NW velocity and time lapsed as a function of its position along the trajectory for a 20nm diameter, 3 μ m long nanowire, which is initially situated at an 8 μ m distance from the electrodes along the inter-electrode center-line [i.e., the (0,-8 μ m) case of panel 'b']. The assumed length / diameter dimensions are representative of NWs in our sample. It is important to note that the NW velocity increases by 2 orders of magnitude as it enters the vicinity of the electrode edges (shown by a dotted line in figure). This step-like increase in velocity is due to the large field gradients that are obtained at electrode edges. As a direct consequence of this rapid increase in velocity, the time taken for a NW to be captured at the electrodes is highly non-linear and decays rapidly as one approaches the electrode edges (Fig. 3(d)). For instance, in this case, the NW will be captured at the electrodes within 0.2504 sec when it starts at an initial location of (0,-3 μ m). On the other hand, the DEP field needs to remain on for 18.62 secs if the NW starts at an initial location of (0,-8 μ m).

Next, we discuss the impact of AC bias and deposition time on the manipulation of NWs. These experiments were carried out at a 10MHz excitation frequency, which represents a low-force excitation field in the sub-crossover frequency regime. As a result, this excitation frequency presents an avenue to precisely control the volumetric region of electrokinetic influence through an appropriate application of other control parameters such as the deposition voltage and time. This argument is

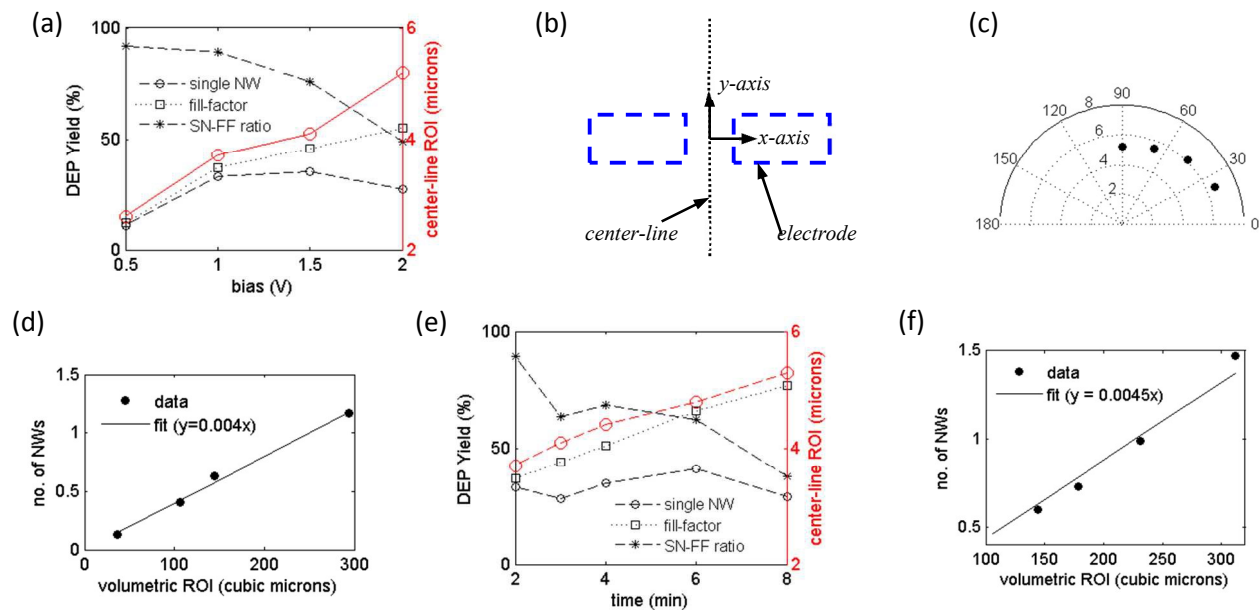


Figure 4. (a-b) DEP results as a function of applied bias at an assembly frequency of 10 MHz (the deposition time was kept constant at 2min). The left y-axis represents the percentage DEP yield in terms of single NW locations, the fill-factor and the SN-FF ratio. The right y-axis represents the calculated center-line, axial ROI for each of the respective deposition conditions. (b) A cartoon of the electrode designs showing the inter-electrode center-line, along which the axial ROI is defined for panels 'a-b'. (c) A polar plot showing the variation of axial ROI as a function of capture radius, i.e., the angular location of the NW at its initial position with respect to the electrodes. In this plot, the r-axis represents the axial ROI in μ m and the θ -axis represents the angular position of the ROI axis. (d) A plot of the experimentally observed number of NWs per electrode location as a function of the computationally estimated volumetric ROI for the deposition conditions in panel 'a'. (e) DEP results as a function of deposition time at an assembly frequency of 10 MHz (the bias was kept constant at 1V for each data point). (f) A plot of the experimentally observed number of NWs per electrode location as a function of the computationally estimated volumetric ROI for the deposition conditions in panel 'e'.

evident from the results of Fig. 4. Fig. 4(a) shows the single NW and fill-factor yields as well as the single NW-to-fill factor (SN-FF) ratio as a function of assembly bias for a deposition time of 2 minutes. As seen in this plot, the fill-factor increases monotonically with increasing bias, as would be expected due to increasing DEP forces. On the other hand, the SN-FF ratio decreases with increases bias starting with a ~90% yield of single NWs at deposition voltages up to 1V. This indicates that while the volumetric ROI increases with increasing DEP forces, there are localized variations in the number of NWs within the volumetric ROI at each electrode location. This is to be expected due to the differences in sizes of NWs within our sample. We have observed NWs with lengths ranging from 1 to 6 μm and diameters ranging from 15nm to 30nm, with very few occasional outliers outside of this predominant range. Assuming a constant density, i.e., a constant mass per unit volume of NWs in the ethanol suspension due to ultrasonication prior to DEP, this indicates a larger number of NWs per unit volume in electrode locations with smaller sized NWs, as compared to locations with larger sized NWs in their volumetric ROI. It is important to note that larger SN-FF ratio at high fill-factor deposition conditions may be obtained through the use of additional strategies, which are designed to limit deposition after the first nanowire is captured. Past reports have employed strategies such as a combined electric field and magnetic field assisted trapping of heterostructured nanowires, which contain a magnetized component in their material system.²³ Another method for improving single nanowire yields has involved lithographically patterned photoresist wells at target sites (with well-widths that accommodate exactly a single nanowire), followed by a post-deposition lift-off of nanowires deposited at undesirable locations.¹³

Fig. 4(a) also plots the computationally estimated center-line, axial ROI for each deposition condition (defined using the right y-axis of this image). It is important to note that this axial ROI represents the farthest distance along the inter-electrode center-line (with respect to the mid-point of the electrode) within which a NW needs to be located in order to be captured by the electrodes. This definition of the center-line ROI axis is schematically illustrated in Fig. 4(b). From Fig. 4(a), we see that the center-line, axial ROI increases from 2.6 μm at 0.5V to 5.2 μm at 2V. This implies that, as the applied bias is increased, NWs located further from the electrodes will be captured and assembled on the chip.

Furthermore, the variation of this axial ROI as function of radial position of the axis is illustrated in the polar plot of Fig. 4(c). From this plot, we find that the axial ROI increases with the radial position of the axis (from 5.2 μm at 0 $^\circ$ to 6.5 μm at 67.5 $^\circ$). Thus, an axial ROI of 5.2 μm represents a conservative estimate for the ROI along any radial location within the plane of the electrodes. It is important to note that our computational models are 2-dimensional approximations of the electrokinetic nanomanipulation system. However, these are valid for not just the x-y plane containing the surface of the electrodes, but also to any cross-sectional plane (in the y-z axis) that contains the electrodes. As a result, it is also valid in the cross-sectional planes that remain within the electrode width, which measures 4 μm in our designs. Since the axial ROI of our DEP operating conditions are on the order of electrode widths, we can approximate the volumetric ROI to be a hemispherical volume, which is centered at the mid-point of the inter-electrode gap

region and has a radius equal to the center-line ROI. Using this approximation, we compute the volumetric ROI (V_{ROI}) as

$$V_{ROI} = \frac{2}{3} \pi r_{ROI}^3 \quad (8)$$

where r_{ROI} represents the center-line ROI. Furthermore, for each deposition condition, we calculate the average number of NWs per electrode location by taking into account the total number of NWs deposited at each of the 100 electrode locations (obtained from SEM images). The variation in this number of NWs (per electrode location) as a function of the volumetric ROI is shown in Fig. 4(d). For a given suspension concentration, the average number of NWs around each electrode location will scale linearly with the volume of suspension around it. We find this relationship to hold in our plot of Fig. 4(d) and the slope of the linear fit to this data, which indicates the number density of NWs per cubic micron of space around the electrodes to be 0.004 NWs per μm^3 .

The experimental results showing the dependence of single NW yield, fill factor and SN-FF ratio on the deposition time is shown in Fig. 4(e). Also, the data represented using the right y-axis of this plot indicates the progressive expansion in center-line ROI with increasing deposition time. Thus, as with the excitation bias, we again find that the NW fill factor increases with increasing ROI. Also, the SN-FF ratio monotonically decreases with increasing ROI due to local variations in the number of NWs per electrode location. For these experiments involving changes in the deposition time, the variation of average number of NWs trapped per electrode location is plotted against the volumetric ROI in Fig. 4(f). This data also exhibits a linear profile, thereby confirming the accuracy of our computational models for the volumetric ROI. Also, we compute the number density of NWs to be 0.0045 per cubic microns. It is interesting to note that the estimate for NW concentration from the time-dependence experiments is within 11.25% of that from bias-dependence experiments. This agreement in estimated NW density in the suspension, from two different sets of experimental data involving changes in AC bias and deposition time, points to the accuracy of our quantitative models and supports our arguments related to the dependence of ROI on the DEP force fields.

Another important consideration in our electrokinetic manipulation experiments is the operation in a sub-crossover frequency regime, which is near the transition from positive to negative DEP. This results in Claussius-Massotti factors, which

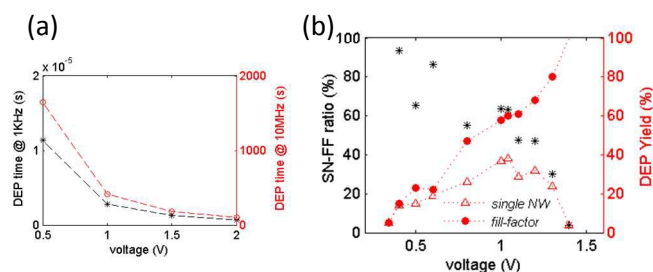


Figure 5. (a) A plot of estimated deposition time for a NW, which is at an initial position of (0,5) μm at the start of DEP. The eight-fold reduction in time deposition time at 1KHz (as compared to the 10 MHz condition) can be observed here. (b) DEP results as a function of voltage at an assembly frequency of 1 KHz and a deposition time of 2 minutes.

are 8-10 orders of magnitude smaller at this sub-crossover regime as compared to the near DC (i.e., 100 to 10KHz) regime. We find that these low forces at the sub-crossover regime result in NW capture times on the order of minutes. On the other hand, at lower frequencies such as 1KHz, the capture times for the same volumetric ROI and same applied bias voltage drop by 8 orders of magnitude (Fig. 5(a)). For instance, the capture time for a NW, which is located 5 μ m away from the electrodes on that electrode pair's center-line axis, is calculated to vary from 11.38 μ secs to 0.71 μ secs when the applied bias changes from 0.5V to 2V. These extremely short capture times associated with these low frequency operating conditions will make it challenging to controllably manipulate and capture single, isolated NWs. This operating condition has not been verified experimentally due to the dominating influence of the double-layer capacitance⁶ on the DEP assembly circuit associated with our floating electrode DEP designs.^{4,6,21} As a result, the actual DEP bias that appears across the suspension will be much lower than applied AC signal (with much of the voltage dropping across the electrical double-layer). Even though a direct comparison of NW deposition as a function of V_{DEP} (DEP bias) cannot be performed at these frequency regimes in the absence of additional data such as impedance spectroscopy measurements, we have experimentally studied the variation in deposition yields as a function of V_{AC} (the AC bias) at 1KHz (Fig. 5(b)). From this plot, it emerges that we find a substantially higher NW deposition as compared to the 10MHz excitation frequency, as can be observed from a 100% NW fill-factor and a 4% SN-FF ratio at 1.4V. For comparison, when we operated at a frequency of 10MHz, we observed a fill factor for 46% and a 76% SN-FF ratio at a slightly higher bias of 1.5V. It is important to note that even though the AC bias, V_{AC} , applied between the biasing electrode and back-gate is nearly the same in both cases, the actual voltage, V_{DEP} , appearing across the suspension is expected to be much lower for the 1KHz. We have still observed a substantially higher NW deposition at the lower frequency, pointing to the extremely large force-fields. Thus, we find that operating in the low force-fields generated within the sub-crossover regime provides an appropriate avenue to manipulate single nanowires within colloidal suspensions.

Conclusions

We have presented pathways to precisely control the region of electrokinetic influence for manipulating single 1-D nano-objects within DEP force fields. We show that electric field excitation in the sub-crossover frequency regime provides an effective avenue to control the electrokinetic ROI. This information, together with complementary techniques reported in past literature such as those involving hydrodynamic flow-fields to achieve uniform density of aligned NWs,¹¹ provides avenues to precisely identify the DEP control parameters such as assembly bias, frequency, and time for predictive deposition of single NWs onto functional nanostructures. In addition, we have determined the dielectric permittivity of the NWs by monitoring their DEP crossover frequency. Finally, we have also presented a new technique to extract the average concentration of NWs in a colloidal suspension from experimental DEP data on NW yields as a function of parameters such as bias voltage and deposition time. These results will enable the design, fabrication and characterization of single nanomaterial platforms based on diverse, functional material systems with multiple morphologies in 1-D (such as nanowires, nanotubes, nanobelts, nanorods and nanoribbons)

for sensing, nanoelectronics, electrocatalysis and electrochemistry applications.

Acknowledgements

This work was partly supported by the National Science Foundation under Grant No. 1266438. EP also acknowledges the support from Drexel University start-up funds. The SEM and AFM imaging were performed at the VCU Nanomaterials Characterization Core (NCC) Facility. We would also like to acknowledge the assistance of Dr. Dmitry Pestov at NCC for his assistance with training activities on the imaging tools. This work was performed, in part, at the Sandia-Los Alamos Center for Integrated Nanotechnologies (CINT), a U.S. Department of Energy, Office of Basic Energy Sciences user facility. The chip nanofabrication activities were performed at CINT under the user proposal U2014A0084. Sandia National Laboratories is a multi-program laboratory operated by Sandia Corporation, a wholly owned subsidiary of Lockheed Martin company, for the U.S. Department of Energy's National Nuclear Security Administration under contract DE-AC04-94AL85000.

Notes and references

^a Department of Mechanical and Nuclear Engineering, Virginia Commonwealth University, Richmond, VA 23284, USA. Email: asubramanian@vcu.edu.

^b Department of Materials Science and Engineering, Drexel University, Philadelphia, PA 19104, USA.

- J. Y. Huang, L. Zhong, C. M. Wang, J. P. Sullivan, W. Xu, L. Q. Zhang, S. C. Mao, N. S. Hudak, X. H. Liu, A. Subramanian, H. Y. Fan, L. Qi, A. Kushima and J. Li, *Science*, 2010, **330**, 1515.
- S. Glassner, C. Zeiner, P. Periwal, T. Baron, E. Bertagnolli and A. Lugstein, *Nano Lett.*, 2014, doi: 10.1021/nl503476t.
- A. Kanwal, S. C. Wang, Y. Ying, R. Cohen, S. Lakshmanan, A. Patlolla, Z. Iqbal, G. A. Thomas and R. C. Farrow, *Electrochem. Comm.*, 2014, **39**, 37.
- A. Subramanian, N. S. Hudak, J. Y. Huang, Y. Zhan, J. Lou and J. P. Sullivan, *Nanotech.*, 2014, **25**, 265402.
- A. Subramanian, A. R. Alt, L. X. Dong, B. E. Kratochvil, C. R. Bolognesi and B. J. Nelson, *ACS Nano*, 2009, **3**, 2953.
- B. R. Burg, V. Bianco, J. Schneider and D. Poulidakos, *J. Appl. Phys.*, 2010, **107**, 14308.
- D. Xu, A. Subramanian, L. X. Dong and B. J. Nelson, *IEEE Trans. Nanotech.*, 2009, **8**, 449.
- A. Subramanian, T. Choi, L. X. Dong, J. Tharian, U. Sennhauser, D. Poulidakos and B. J. Nelson, *Appl. Phys. A: Matl. Science and Proc.*, 2007, **89**, 133.
- A. Subramanian, L. X. Dong, A. Ferreira and B. J. Nelson, *Appl. Phys. Lett.*, 2010, **96**, 073116.
- B. R. Burg and D. Poulidakos, *J. Mat. Res.*, 2011, **26**, 1561.
- E. M. freer, O. Grachev, X. F. Duan, S. Martin and D. P. Stumbo, *Nat. Nanotech.*, 2010, **5**, 525.
- S. Raychaudhuri, S. A. Dayeh, D. Wang and E. T. Yu, *Nano Lett.*, 2009, **9**, 2260.
- M. Li, R. B. Bhiladvala, T. J. Morrow, J. A. Sioss, K.-K. Lew, J. M. Redwing, C. D. Keating and T. S. Mayer, *Nat. Nanotech.*, 2008, **3**, 88.

- 14 T. J. Morrow, M. Li, J. Kim, T. S. Mayer and C. D. Keating, *Science*, 2009, **323**, 352.
- 15 S. J. Papadakis, J. A. Hoffmann, D. Deglau, A. Chen, P. Tyagi and D. H. Gracias, *Nanoscale*, 2011, **3**, 1059.
- 16 P. A. Smith, C. D. Nordquist, T. N. Jackson, T. S. Mayer, B. R. Martin, J. Mbindyo and T. E. Mallouk, *Appl. Phys. Lett.*, 2000, **77**, 1399.
- 17 N. R. Palapati, A. Muth, Y. Zhu, C. Wang and A. Subramanian, *ASME J. of Nanotech. in Eng. and Med.*, 2014, **5**, 021001.
- 18 M. Liu, J. Lagdani, H. Imrane, C. Pettiford, J. Lou, S. Yoon, V. G. Harris, C. Vittoria and N. X. Sun, *Appl. Phys. Lett.*, 2007, **90**, 103105.
- 19 D. A. Brown, J.-H. Kim, H.-B. Lee, G. Fotouhi, K.-H. Lee, W. K. Liu and J.-H. Chung, *Sensors*, 2012, **12**, 5725.
- 20 M. Dimald and P. Boggild, *Nanotech.*, **16**, 2005, 759.
- 21 B. Krupke, F. Hennrich, H. B. Weber, M. M. Kappes and V. M. Lohneysen, *Nano Lett.*, 2003, **3**, 1019.
- 22 L. A. Nagahara, I. Amlani, J. Lewenstein and R. K. Tsui, *Appl. Phys. Lett.*, 2002, **80**, 3826.
- 23 K. Kim, X. B. Xu, J. H. Guo and D. L. Fan, *Nat. Comm.*, 2014, **5**, 3632.
- 24 Z. Gao, J. Wang, G. Wan, Y. Zou and Qian, *J. Cryst. Growth*, 2005, **279**, 415.
- 25 J. A. Riddick and W. B. Bunger, *Organic Solvents*, New York, U.S.: Wiley-Interscience, 1970.
- 26 D.-K. Kwon, T. Akiyoshi, H. Lee and M. T. Lanagan, *J. Am. Ceram. Soc.*, 2008, **91**, 906.
- 27 H. Morgan and N. G. Green, *AC Electrokinetics: Colloids and Nanoparticles*, Hertfordshire, U.K.: Research Studies Press, 2003.
- 28 H. Ding, W. Liu, J. Shao, Y. Ding, L. Zhang and J. Niu, *Langmuir*, 2013, **29**, 12093.
- 29 T. B. Jones, *Electromechanics of Particles*, Cambridge, U.K.: Cambridge Univ. Press, 1995.
- 30 M. Dimald and P. Boggild, *Nanotech.*, 2004, **15**, 1095.
- 31 R. Krupke, F. Hennrich, H. V. Lohneysen and M. M. Kappes, *Science*, 2003, **301**, 344.
- 32 H. Guan, Y. Wang, G. Chen and J. Zhu, *Powder Tech.*, 2012, **224**, 356.
- 33 Y. K. Ren, D. Morganti, H. Y. Jiang, A. Ramos and H. Morgan, *Langmuir*, 2011, **27**, 2128.
- 34 S. H. Koenig, *Biopolymers*, 1975, **14**, 2421.
- 35 S. C. Harding, M. Dampier and A. J. Rowe, *IRCS Med. Sci.*, 1979, **7**, 1813.
- 36 E. W. Small and I. Isenberg, *Biopolymers*, 1977, **16**, 1907.